Postprint of: Skarżyński Ł., Marzec I., Shear fracture of longitudinally reinforced concrete beams under bending using Digital Image Correlation and FE simulations with concrete micro-structure based on X-ray micro-computed tomography images, Construction and Building Materials, Vol. 274 (2021), 122116, DOI: 10.1016/j.conbuildmat.2020.122116

Shear fracture of longitudinally reinforced concrete beams under bending using Digital Image Correlation and FE simulations with concrete micro-structure based on X-ray micro-computed tomography images

Łukasz Skarżyński and Ireneusz Marzec

Faculty of Civil and Environmental Engineering, Gdańsk University of Technology, Narutowicza 11/12, 80-233 Gdansk, Poland, Email: lskarzyn@pg.edu.pl, irek@pg.edu.pl

Abstract

The paper presents experimental and numerical investigations of the shear fracture in rectangular concrete beams longitudinally reinforced with steel or basalt bar under quasi-static three point bending. Shear fracture process zone formation and development on the surface of beams was investigated by Digital Image Correlation (DIC) whereas thorough analyses of 3D material micro-structure, air voids, width and curvature of shear cracking were carried out by X-ray micro-computed tomography (micro-CT). Moreover, the 2D shear fracture patterns in beams were numerically simulated with the finite element method (FEM) using isotropic coupled elasto-plastic-damage constitutive model for concrete enhanced by a characteristic length of micro-structure. Concrete meso-structure was modelled as a random heterogeneous four-phase material composed of aggregate particles, cement matrix, ITZ zones and air voids on the basis of X-ray micro-CT images. Experimental and numerical results revealed a satisfactory agreement regarding to the mechanism of failure, load-bearing capacity as well as cracking pattern.

Keywords: Damage mechanics, Digital Image Correlation, Shear fracture, Meso-scale finite element method (FEM), X-ray micro-CT

1. Introduction

Shear failure is one of the ways of destruction of reinforced concrete elements subjected to bending, mainly in the nearest neighbourhood of the support zones. This type of failure may results in a reduction of the load capacity based on the longitudinal reinforcement and is particularly dangerous in structures without transversal reinforcement. The issue of estimating the shear capacity of bending elements is one of the most complex phenomenon in reinforced concrete theory due to the complexity of the failure mechanism in the support area that is caused by the simultaneous occurrence of bending moment and shear force. Experimental research in this field started, on a large scale, in the mid-twentieth century [1-12] and it is still continued which indicates that the problem of safe and economical shear dimensioning has not been satisfactory resolved and is still valid. An extensive database of experimental research results as well as new theoretical works result in and increasingly in-depth description of the mechanism of destruction of reinforced concrete elements and the emergence of new calculation methods for estimating material bearing capacity. Significant changes in this respect can be observed, among others, in the dimensioning of bended elements taking into account shear forces, which is commonly called shear dimensioning. The understanding of a shear phenomenon is of a major importance to ensure safety of the structure and to optimize material behaviour [13-19]. Standard rules for dimensioning reinforced concrete elements are also evolving [20-23].

Shear cracking formation and evolution can be observed by my means of Digital Image Correlation. In fact, DIC is one of the most popular techniques due to its simplicity and low cost, however, no information about internal material micro-structure and properties (width and shape) of fracturing could be obtained. Up to now, our experimental studies allowed to successfully capture fracture zone development and its evolution using Digital Image Correlation (DIC) during different mechanisms:

plain concrete subjected to three-point bending [24], plain concrete under tension splitting [25], steel or basalt fibrous concrete during wedge splitting [26, 27]. However, in order to broaden the horizons about internal material micro-structure concerning, for instance, shape and distribution of air voids and aggregate particles as well as gather more valuable data about width and curvature of shear cracks, 3D analyses were carried out by X-ray micro-computed tomography. The recent use of X-ray micro-CT has gained apparent success in obtaining the real structure or phases in cement-based materials like concrete. Our tomography system SkyScan 1173 has already been successfully used for observations of the evolution of a concrete fracture process during: three-point bending in plain concrete [24], tension splitting in plain concrete [25], uniaxial compression in plain concrete [28], compressive fatigue in plain concrete [29], three-point bending in plain concrete under constant scanning [30] and for steel or basalt fibrous concrete subjected to wedge splitting [26, 27]. X-ray micro-computed technique is also very popular technique of fracture investigations among other researchers [31-38].

Simultaneously, in FE simulations of reinforced concrete members the complexity of failure mechanisms and crack pattern has to be incorporated as well. Within continuum mechanics, localisation zones (i.e. cracks and shear zones) can be modelled with two alternative ways i.e. using classical Finite Element Method (FEM) where displacement field continuity is not violated e.g. [39-44] or eXtended Finite Element Method (XFEM) where description of cracks/shear zones in form of zero width displacement jumps can be introduced with aid of e.g. interface cohesive elements [45-47] or strong discontinuity approach [48-49]. Since, in RC members several different failure mechanisms can be observed: steel yielding, concrete cracking in tension, concrete crushing in compression and shear failure modes, the observed crack pattern is usually very complex. In contrast to plain concrete, cracks are not independent but they join and intersect. Thus, FEM models are more commonly used in numerical simulations of RC members, while application of discrete cracks is less popular. Constitutive laws for concrete within FEM incorporate strain softening into material description. It causes the mesh-dependency problem of numerical calculations because the boundary value problem becomes ill-posed. To handle this issue classical continuum laws have to be enriched with a characteristic length. The characteristic length that reflects the heterogeneous meso-structure of the material can be taken into account in constitutive equations by applying, for instance, the non-local theory in the integral form that is simultaneously one of the most valuable and physical methods of regularization for heterogeneous materials. The heterogeneity of tested material has a strong impact on the local phenomena such as the mechanism of the initiation, growth and formation of fracture which finally are responsible for the macroscopic behaviour of material. Thus, to properly describe fracture, it is necessary to take into account realistic material micro-structure while FE modelling. At the meso-scale, four phases like cement matrix, aggregate particles, interfacial transition zones ITZs and macro-voids can be separated. The material behaviour at the meso-scale may be described with finite element FE models [50-53] and discrete models [28, 54-57] with the material meso-structure directly taken from micro-CT images.

2. Significance of research

The current paper is experimentally and numerically oriented. Presented research, concerning concrete reinforced with steel or basalt bar, is an extension of our previous experimental and numerical investigations of fracture properties that were carried out for plain or fiber reinforced concrete [24-30]. The micro-CT images were adopted to create the model of concrete with actual meso-structure. Each material component in the image-based model was segmented and its own mechanical parameters were defined. Such model was incorporated into FE modelling to numerically evaluate the material strength and fracture evolution process. This knowledge is important to better understand a fracture process for enhancing life of reinforced concrete members and structures. Summarizing, there are 2 main objectives of this study that also represent its novelties:

(1) Detailed and thorough experimental investigations of a complicated shear fracture process conditions in reinforced concrete beams under bending using 2D Digital Image Correlation and 3D X-ray micro-CT computed tomography.

(2) FE simulations of reinforced concrete beams subjected to 3-point bending using a meso-scale continuum non-local four-phase model of concrete assembled from aggregate grains, cement matrix, ITZ zones and air voids. The geometry of concrete micro-structure was directly taken from X-ray micro-CT images.

3. Experimental program

3.1. Specimen preparation

The used aggregate sieve curve and mix proportions are depicted in Figure 1 and Table 1. The sand point was assumed to be 41% and the water to cement ratio was established at w/c=0.50. The aggregate grain curve was located between boundary curves that ensure proper workability and consistency of fresh concrete mix with low demand for cement and water as well as minimal air content. A well-designed grain size curve reduces also shrinkage strain of a fresh concrete during first stage of hardening.

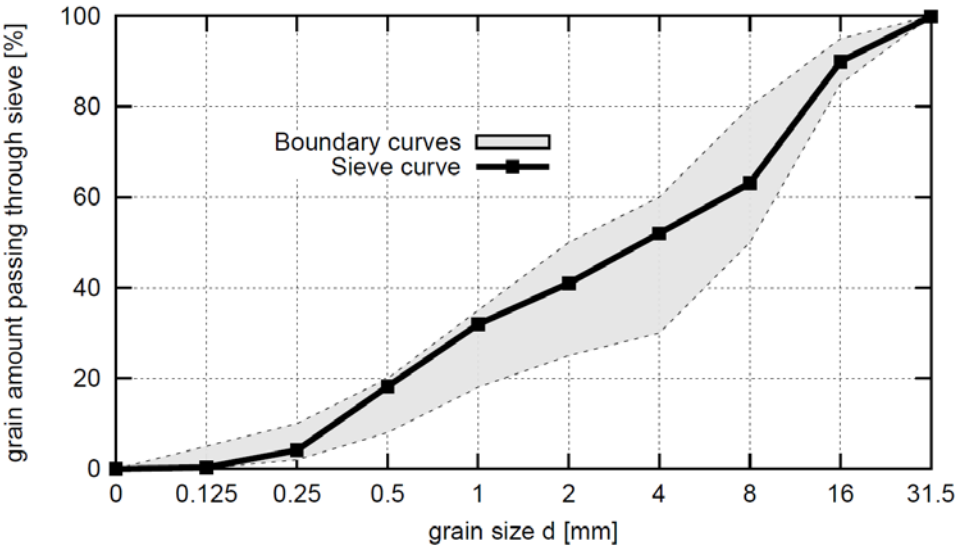

Figure 1: Distribution of aggregate particles

Table 1: Concrete recipe details

Concrete components	**Concrete mix** (d_{50}=2 mm, d_{max}=16 mm)
Cement CEM II/A-LL 42.5R (c)	300 kg/m^3
Sand (0 - 2 mm)	735 kg/m^3
Gravel aggregate (2 - 8 mm)	430 kg/m^3
Gravel aggregate (8 - 16 mm)	665 kg/m^3
Superplasticizer (s)	1.8 kg/m^3
Water (w)	150 kg/m^3

Before molding procedure, the fresh concrete mix properties were validated on the basis of Vebe slump test, Vebe time test and air content pressure test [58]. Tests revealed appropriate concrete mix workability and air content. Both these parameters are very important since they influence final properties of hardened concrete such as strength, permeability and durability. Properties of fresh concrete used in experiments are presented in Table 2.

Table 2: Properties of fresh concrete mix

Concrete mix	Temperature [^{0}C]	Vebe slump test [mm]	Vebe time [s]	Air content [%]	Density [kg/m^3]
Plain concrete mix (Table 1)	14.5	130	3.40	3.24	2322.0

Finally, 2 cubic concrete blocks with dimensions of 500×500×200 mm reinforced with steel or basalt bar of diameter equal 8 mm were prepared. The reinforcement ratio value was ρ=2.1%. Due to the declaration of conformity of the manufacturers the mechanical properties of reinforcement were as follows: the tensile strength of basalt f_{yb}=1100 MPa, the tensile strength of steel f_{ys}=650 MPa. modulus of elasticity of composite basalt bars was E_b=70 GPa and the modulus of elasticity of steel E_s=200 GPa. The basalt bars contained 80% of the basalt fibers and 20% of the epoxy resin. For the first 7 days, blocks were stored in a climatic chamber at temperature about 20^{0}C and humidity 95% [59] to avoid the surface evaporation and autogenous shrinkage. Afterwards, the rectangular reinforced concrete beams (length 160 mm, span L=120 mm, height 60 mm, effective height d=45 mm, width b=40 mm) were cut out on the 28th day after concreting from the prisms with the tolerance of dimensions equal ±0.2 mm. The distance of force from the support was assumed to be a=60 mm therefore the ratio between the beam shear span a and effective height d was equal $\eta = a/d$=60/45=1.33 (Figure 2) The concrete cover from the bar centre to the concrete surface was 15 mm. A relatively small geometry of reinforced concrete specimens (resulting also in a rather thin concrete cover) were used in order to provide the ability to scan them in the micro-CT system. Geometry of the tested specimens is presented in Figure 2.

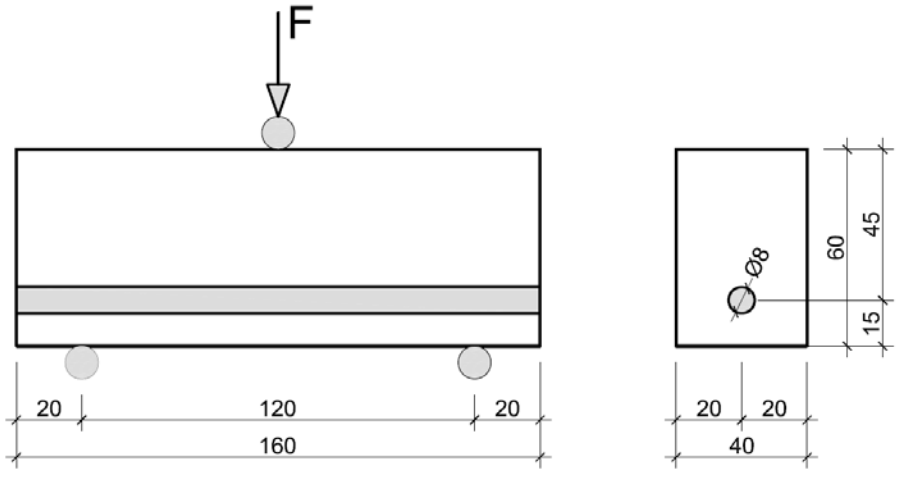

Figure 2: Geometry of the concrete specimen reinforced with steel or basalt bar

Mechanical tests (on plain concrete specimens) carried out on 6 cubic specimens with the dimensions of 15×15×15 cm on 28th day after concreting, revealed that the average uniaxial compressive strength [60] was equal f_c=47.60 MPa with the standard deviation of 1.66 MPa and the average splitting strength [61] was equal f_{ct}=3.46 MPa with the standard deviation of 0.19 MPa. The Young's modulus equal E=36.1 GPa with the standard deviation of 2.29 GPa and the Poisson's ratio equal

υ=0.22 with the standard deviation of 0.03 were obtained on the basis of tests carried on 3 cylinder specimens 15×30 cm. The average flexural strength [62], tested on 3 concrete beams 15×15×60 cm, was f_{cf}=3.60 MPa with the standard deviation of 0.2 MPa.

3.2. Digital Image Correlation

Digital camera NIKON D800 with 36 megapixel matrix was used to visualise 2D fracture process evolution in reinforced concrete beams subjected to 3-point bending by means of Digital Image Correlation (DIC). Photographed area was about 160×80 mm that results in a pixel size equal 15 μm and length resolution equal approximately 65 pixel/mm, however, an analysed area was limited to 120×60 mm. Digital camera was placed perpendicularly to the sprayed surface of the tested beams. The digital images were taken continuously during entire test with 6 seconds interval. Testing station used for DIC experiments is presented in Figure 3.

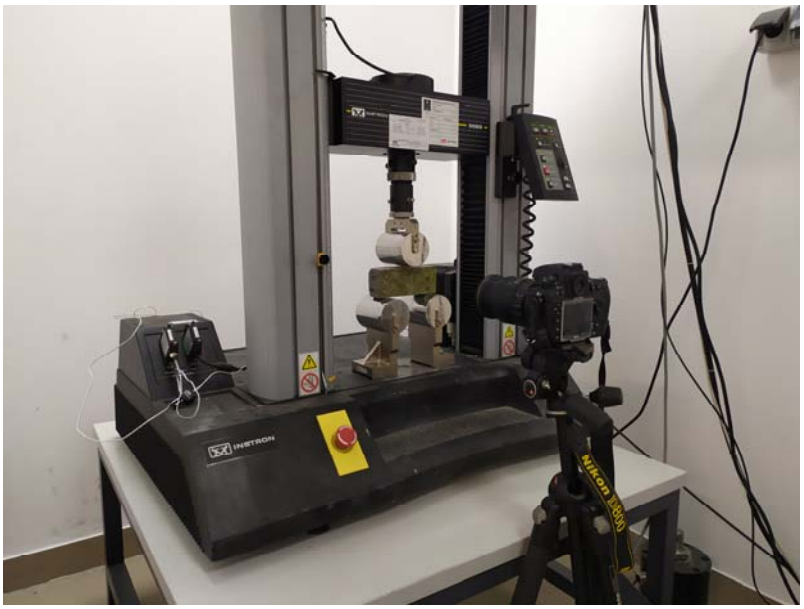

Figure 3: View on the DIC testing station. Digital NIKON D800 camera is mounted on a tripod perpendicularly to the concrete beam placed in Instron 5569 static machine

3.3. X-ray micro-CT scanning

X-ray micro-CT SkyScan 1173 scanner with 0.2 mm brass filter was used to investigate 3D material micro-structure and fracture properties. The X-ray source voltage and the current were equal 130 keV and 61 μA, respectively. The voxel size of the X-ray micro-CT was 39.68 microns whereas the shutter speed equaled 5000 ms. The sample was scanned at 360 degrees with a single rotation step of 0.4 degrees. An oversize scanning option was used to visualise entire beam samples that was originally too long to fit in the micro-CT field of view. The samples were scanned in 2 sub-scans by moving the rotation table down after the first sub-scan was finished. The reconstruction was done sub-scan by sub-scan with the necessary adjustment in the file sequences to form a complete stack of 3D volume ideally. Experimental procedure started from initial micro-CT scan of non-cracked samples in order to gather all necessary information, concerning initial porosity and material microstructure. After the mechanical testing, entire procedure was repeated for a cracked samples. Testing station used for micro-CT experiments is presented in Figure 4.

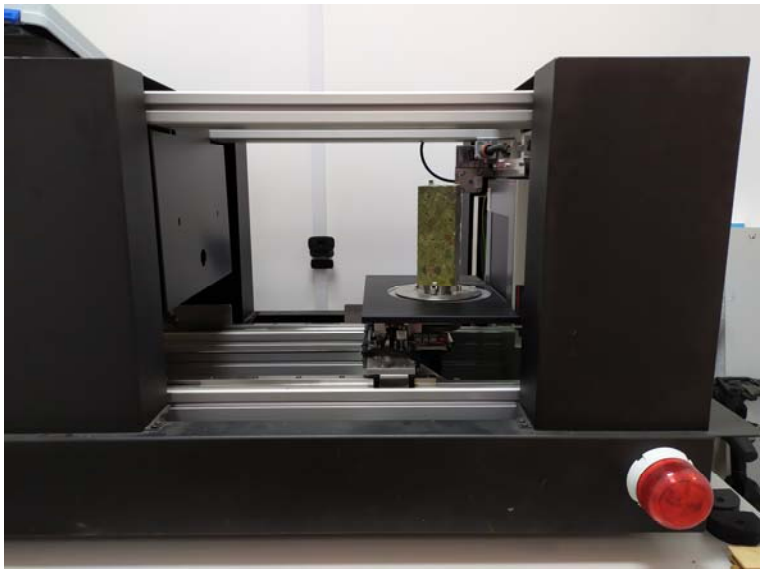

Figure 4: Tested sample mounted on the rotation table of micro-CT 1173 Skyscan X-ray micro-tomograph testing station

3.4. Numerical Finite Element approach

Non-local model for concrete

The FE analyses were conducted with a coupled isotropic elasto-plastic-damage approach for concrete. The comprehensive description, advantages and drawbacks of the above mentioned model were outlined in detail in [63]. This constitutive model has already been successfully applied to various RC members, e.g. RC beams under mixed shear-tension failure [64], and composite RC-EPS slabs and walls under shear failure [65, 66]. The constitutive law couples continuum damage mechanics with elasto-plasticity. The idea follows the proposal by Pamin and de Borst [67] and is based on strain equivalence hypothesis. Elasto-plasticity is defined in effective stress space. Rankine and Drucker-Prager criteria with linear hardening (with the modulus equal to $E/2$ where E stands for Young modulus) are assumed for elasto-plasticity. The softening of the material is described via isotropic damage with an equivalent strain measure $\tilde{\varepsilon}$ defined in total strains taken after Mazars [68]:

$$\tilde{\varepsilon} = \sqrt{\sum \langle \varepsilon_i \rangle^2} \tag{1}$$

where ε_i is a principal strain. The state variable κ and two additional quantities κ_t and κ_c to describe stiffness degradation in tension and softening, respectively, are defined as:

$$\kappa = \max_{\tau \le t} \tilde{\varepsilon}(\tau), \qquad \kappa_t = r\kappa, \qquad \kappa_c = (1-r)\kappa \tag{2}$$

where r is a triaxiality factor [69, 70] calculated via:

$$r(\boldsymbol{\sigma}) = \frac{\sum \langle \sigma_i \rangle}{\sum |\sigma_i|} \tag{3}$$

where $\langle \sigma_i \rangle$ stands for a positive value of principal stress σ_i and $|\sigma_i|$ denotes an absolute value of a principal stress σ_i.

The degradation parameter D is described via the following formula:

$$D = 1 - \left(1 - s_c D_t\right)\left(1 - s_t D_c\right) \tag{4}$$

where s_c and s_t are splitting functions. The degradation parameter in tension D_t is defined as [71]:

$$D_t = 1 - \frac{\kappa_0}{\kappa_t}\left(1 - \alpha + \alpha \exp\left(-\beta\left(\kappa_t - \kappa_0\right)\right)\right) \tag{5}$$

with state variable κ_t and parameters κ_0, α, β. The degradation parameter in compression is calculated using the relationship after [72]:

$$D_c = 1 - \left(1 - \frac{\kappa_0}{\kappa_c}\right)\left(0.01\frac{\kappa_0}{\kappa_c}\right)^{\eta_1} - \left(\frac{\kappa_0}{\kappa_c}\right)^{\eta_2} \exp\left(-\delta_c\left(\kappa_c - \kappa_0\right)\right) \tag{6}$$

with state variables η_1, η_2 and δ_c.

Note that the same value of κ_0 is used to calculated both degradation parameters D_t and D_c. Full description and more details of the performance of the model can be found in [63].

Numerical simulations with classical continuum constitutive laws with softening do not produce reliable results. Obtained outcomes are mesh dependent, because the boundary value problem is ill-posed. In order to restore the well posedness of the boundary value problem information about a characteristic length of the micro-structure has to be added. One of the possibilities comes with the integral non-local theory. It replaces a local value of the variable controlling the softening of the material by its non-local counterpart, calculated as an averaged quantity over neighbours.

To introduce regularization into the formulation only the damage part was "made non-local" since the elasto-plastic part of model produces no softening (it includes only hardening). Thus, the damage part (which is responsible for material softening) was modified by replacing the local equivalent strain measure by its non-local counterpart calculated according to the formula:

$$\overline{\varepsilon}\left(\boldsymbol{x}\right) = \frac{\int_V \omega\left(\left\|\boldsymbol{x} - \boldsymbol{\xi}\right\|\right)\tilde{\varepsilon}\left(\boldsymbol{\xi}\right) d\boldsymbol{\xi}}{\int_V \omega\left(\left\|\boldsymbol{x} - \boldsymbol{\xi}\right\|\right) d\boldsymbol{\xi}} \tag{7}$$

Where $\boldsymbol{x}$ is a considered point and $\boldsymbol{\xi}$ are neighbour points. As a weighting function $\boldsymbol{\omega}$ Gauss distribution function is used:

$$\omega\left(r\right) = \frac{1}{l_c\sqrt{\pi}} \exp\left(-\left(\frac{r}{l_c}\right)^2\right) \tag{8}$$

where l_c denotes the characteristic length of the microstructure.

It should be noted that in practice the averaging is restricted to the small area around the considered point (the influence of neighbor points at the distance of r=3× l_c is only of 0.01%). To calibrate the non-local model, usually, the inverse identification process of experimental data may be used to

determine a value of l_c. The nonlocal averaging should also properly describe the fracture process zone experimentally observed in heterogeneous materials [73]. Additionally, in order to counteract excessive energy dissipation, additional improvement such as distance-based and stress-based model or local correction approach need to be incorporated [74]. In turn, when calculating non-local quantities close to internal barrier the so-called "shading effect" is also taken into account.

FE input data

In FE-calculation two different models for concrete where assumed to simulate the evolution of the localized zones i.e. macro-scale and meso-scale model. The general scheme for both approaches is presented in Figure 6. The FE discretization for macro-scale approach is presented in Figure 6a. The FE mesh included 9600 plane stress square elements for concrete and 160 one-dimensional truss elements for reinforcing bars. The size of finite elements was about 1 mm, and it was smaller than the characteristic length l_c=1.5 mm. For describing the interaction between concrete and reinforcement, a bond-slip law followed CEB-FIP Code [75] was defined. The CEB-FIB bond-slip law describes relationship between the bond shear stress τ_b and slip δ with the following formulae:

$$\tau_b = \begin{cases} \tau_{\max}\left(\dfrac{\delta}{\delta_1}\right)^{\alpha} & 0 < \delta \le \delta_1 \\ \tau_{\max} & \delta_1 < \delta \le \delta_2 \\ \tau_{\max}\left(\tau_{\max} - \tau_f\right)\dfrac{\delta - \delta_1}{\delta_3 - \delta_2} & \delta_2 < \delta \le \delta_3 \\ \tau_f & \delta_3 < \delta \end{cases} \tag{9}$$

This bond-slip law describes 4 different phases by taking hardening/softening into account in the relationship. Based on preliminary simulations [63] the following bond parameters were taken: τ_{max}=10 MPa, τ_f=3 MPa, δ_1=1 mm, δ_2=2 mm, δ_3=5 mm and α=0.2. The graphical interpretation of assumed bond-slip law for given set of material parameters is depicted on Figure 5.

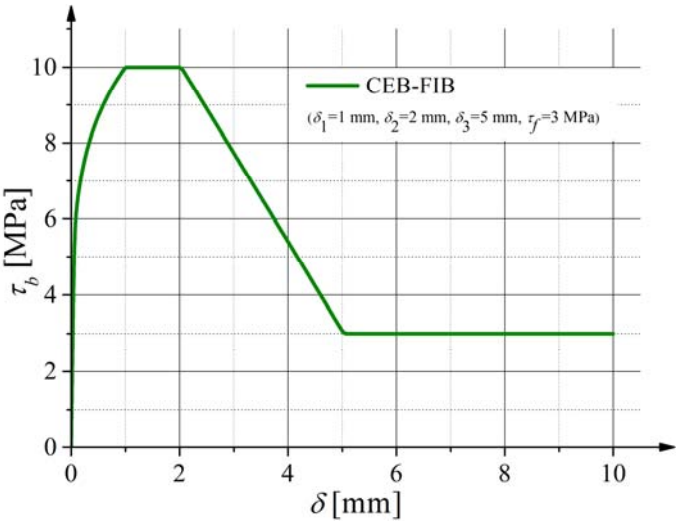

Figure 5: Bond stress-slip relationship τ_b= f(δ) by CEB-FIP code, for assumed material parameters

The bond interaction was assumed as an interface with a zero thickness along a contact line where the relationship between the shear traction and slip was defined. In turn, the meso-scale approach takes into account concrete heterogeneity. The exemplary FE mesh with distinguished four phases: angularly-shaped aggregate particles (marked in brown) , cement matrix (marked in blue), ITZ zones

(marked in green) and air voids (white round spots) is shown in Figure 6b. The aggregate grains (assumed as the particles with the size ≥ 2.0 mm) were embedded in the specimen and were described by a linear elastic model. The location, shape, size and distribution of aggregate grains and air voids for all four beams directly corresponded to the concrete images from micro-CT scanning. The images taken in the middle of cross section were assumed as a basis to build the geometry of the FE meshes. The width of ITZs around aggregate particles was constant – 0.5 mm (based on [54]). The FE-meshes included in total about 300.000 triangular elements. The size of finite elements was: 0.2–0.7 mm (aggregate), 0.2–0.7 mm (cement matrix) and 0.2 mm (ITZs) (Figure 6b). Thus, for each phase the size of finite elements was smaller than the characteristic length l_c=1.5 mm. The size of the characteristic length was based on our previous experiments on concrete beams [24]. In order to simplify the FE mesh creation the large air voids (with diameter 0.8–4 mm) were only taken into account, since the effect of small air voids on the crack propagation was negligible [54]. As a consequence the area of air voids (modelled as the empty spots) in the numerical models were smaller by about 40% as compared with the measured one. The reinforcement bar was also modeled with 2D triangular elements (Figure 6b). The calculations were carried out under plane stress conditions. Similarly as for macro-scale model a bond-slip law followed CEB-FIP Code [75] was defined to describe interaction between concrete and reinforcement. For both approaches the punctual supports and the point of application of load were induced with aid of small steel plates in order to avoid local concrete crushing. FE analyses were conducted with the coupled isotropic elasto-plastic-damage model for concrete. The material parameters for each individual phase of meso-scale approach: aggregate, cement matrix and ITZs are presented in Table 3. Additionally, plastic hardening moduli H_p=18 GPa was assumed for elasto-plasticity. The modulus of elasticity of aggregate grains (composed of 55% of granite, 30% of limestone, 13% of sandstone and 2% of basalt) was calculated as the mean value of the moduli of the individual rock components [54]. In turn, for macro-scale approach the material parameters for concrete were assumed similar as for cement matrix in meso-scale approach. The material constants, for meso-scale approach, were determined by means of two independent simple monotonic tests: uniaxial compression test and three-point bending. In turn, assumed for macro-scale approach, the material parameters for concrete similar as for cement matrix in meso-scale approach were driven by our preliminary calculations. This simplification provides a satisfactory agreement between both approaches regarding calculated load-displacement curves. In order to simulate the behaviour of steel and basalt bar, an elastic-perfectly plastic constitutive model was assumed. The modulus of elasticity E_s=200 GPa and E_b=70 GPa and yield stress σ_{ys}=650 MPa and σ_{yb}=1100 MPa were assumed for steel and basalt, respectively.

All numerical calculations were executed in Abaqus Standard commercial code [76]. To introduce the constitutive model for concrete, model for reinforcement, bond-slip law and non-local averaging the user constitutive law definition (UMAT) and user element definition (UEL) subroutines were introduced.

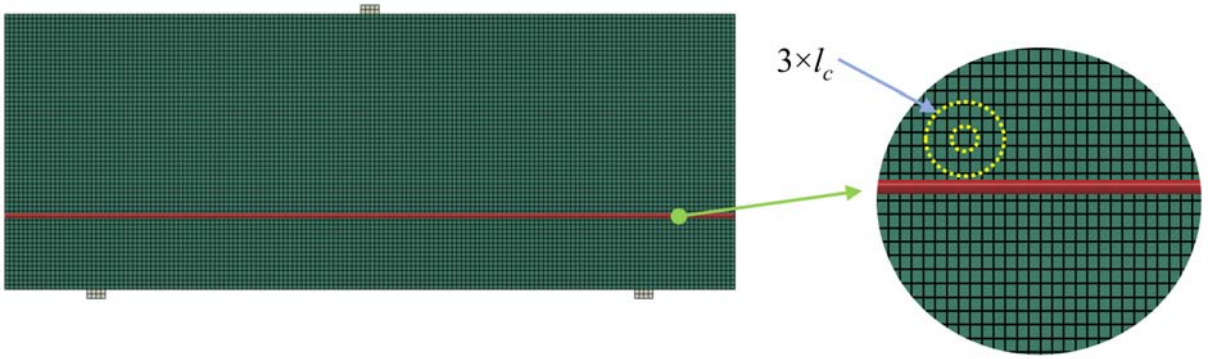

(a)

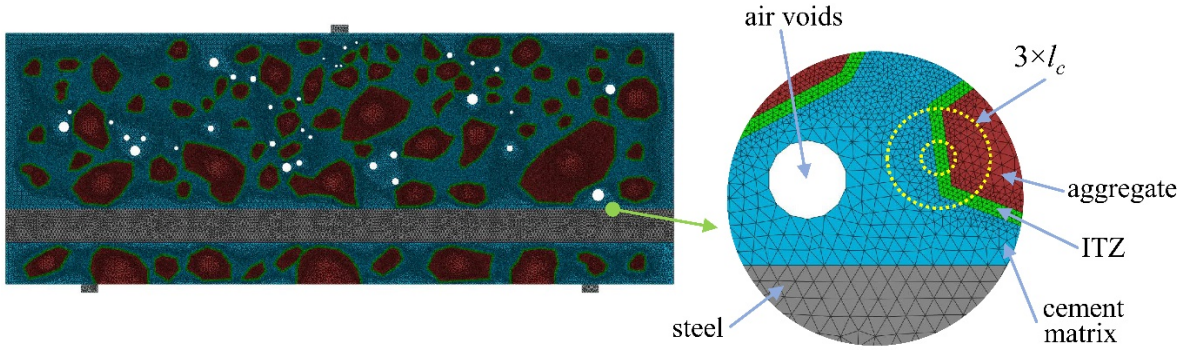

(b)

Figure 6: Exemplary FE mesh discretization for: (a) macro-scale model and (b) meso-scale model

Table 3: Material parameters assumed in FE calculations on meso-scale approach

Material constant	Aggregate	Cement matrix	ITZ
Modulus of elasticity E (GPa)	47.2	36.1	18.1
Poisson's ratio ν (-)	0.2	0.2	0.2
Initial yield stress (tension) σ_{yt}^0 (MPa)		3.5	2.8
Initial yield stress (compression) σ_{yc}^0 (MPa)		50	40
State variable κ (-)	-	8.0×10^{-5}	5.9×10^{-5}
Damage parameter (tension) α (-)	-	0.95	0.95
Damage parameter (tension) β (-)	-	150	150
Damage parameter (compression) η_1 (-)	-	1.0	1.0
Damage parameter (compression) η_2 (-)	-	0.15	0.15
Damage parameter (compression) δ_c (-)		150	150

4. Experimental results and discussion

4.1. Initial void analysis

Figures 7 and 8 and Table 4 show the initial 3D air void content and air void distribution in non-cracked steel and basalt reinforced concrete measured by micro-CT. Air voids were separated using threshold value between 0-60 (within the whole 0-255 scale) and were treated in two ways i.e. as open pores that cross the boundaries of VOI (Volume of Interest) or closed pores that are entirely embedded in VOI. Based on that assumption, air volume in non-cracked concrete specimens reinforced with steel bar varied from 7418.98 mm^3 to 7564.93 mm^3 that corresponds to 3.05% and 3.11% of total air volume, whereas closed porosity varied from 2.45% to 2.55% and open porosity varied from 0.56% to 0.60%. Similarly, air volume in non-cracked concrete specimens reinforced with basalt bar varied from 7969.58 mm^3 to 8362.21 mm^3 that corresponds to 3.45% and 3.62% of total air volume, whereas closed porosity varied from 2.63% to 2.92% and open porosity varied from 0.70% and 0.82%. Thus, it could be noticed that total porosity of concrete beams reinforced with steel bar was smaller by about 15% than porosity of concrete beams reinforced with basalt bar. However, measured porosity values are quite similar and, moreover, show a satisfactory agreement with air content of fresh concrete obtained in the air pressure method. Figure 7b shows that despite careful concreting and compacting of fresh mix some air is left along the steel bar ribs. Presence of

air along the steel bar ribs can lead to the deterioration of contact between concrete and reinforcement. This phenomenon was not observed in terms of basalt bar (Figure 8b).

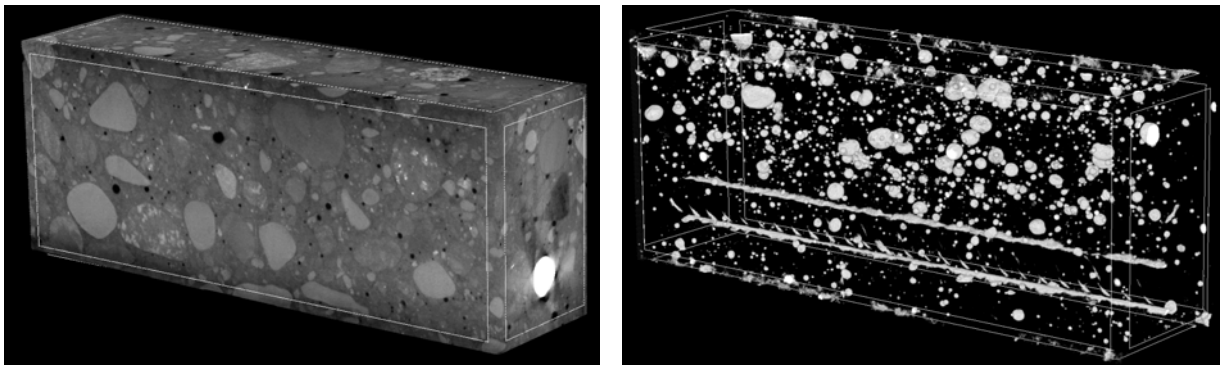

(a) (b)

Figure 7: Non-cracked images of steel reinforced concrete beam by 3D micro-CT: (a) general view and (b) distribution of pores

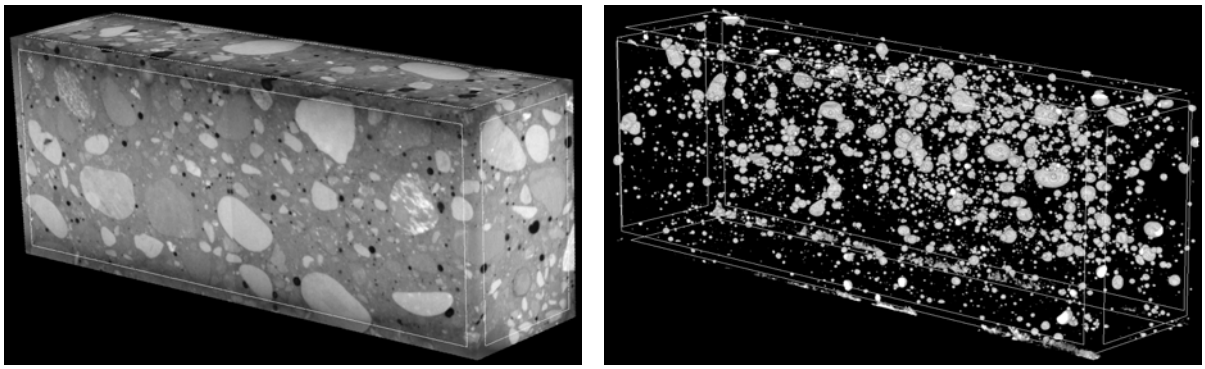

(a) (b)

Figure 8: Non-cracked images of basalt reinforced concrete beam by 3D micro-CT: (a) general view and (b) distribution of pores

Table 4: Air void analysis in non-cracked specimens by micro-CT

Specimen number	Volume of pores [mm^3]	Volume of pores [%] within entire sample volume	Volume of closed pores [%] within entire sample volume	Volume of open pores [%] within entire sample volume
Steel #1	7418.98	3.05	2.45	0.60
Steel #2	7564.93	3.11	2.55	0.56
Basalt #1	8391.96	3.45	2.63	0.82
Basalt #2	8805.48	3.62	2.92	0.70

4.2. Material strength

The quasi-static tests with reinforced concrete beams were performed with a controlled displacement rate of 0.05 mm/min. Figure 9 presents vertical force F versus deflection u curves obtained for concrete reinforced with steel or basalt bar subjected to three-point bending. Maximum vertical force of concrete reinforced with steel bar was 12.41 kN (u =1 .33 mm) and 11.33 kN (u=0.87 mm) whereas of concrete reinforced with basalt bar was 10.75 kN (u =1.07 mm) and 10.29 kN

(u= 1.57 mm). It means, that average deflection in concrete beams reinforced with basal bars equal 1.32 mm was about 20% higher than the average deflection in concrete beams reinforced with steel bar equal 1.10 mm. Initially one or two bending cracks appeared close to the mid-span for all tested beams. Then, inclined shear cracks occurred that continuously evolved in length and width along with the deformation process. Tests were stopped before failure in order to allow beams to be scanned in one piece in micro-CT. However, after scanning beams were once again loaded in order to observe failure mechanism. In all cases, failure took place in a rapid brittle way due to a diagonal shear crack moving through the beam compressive zone towards the loading point.

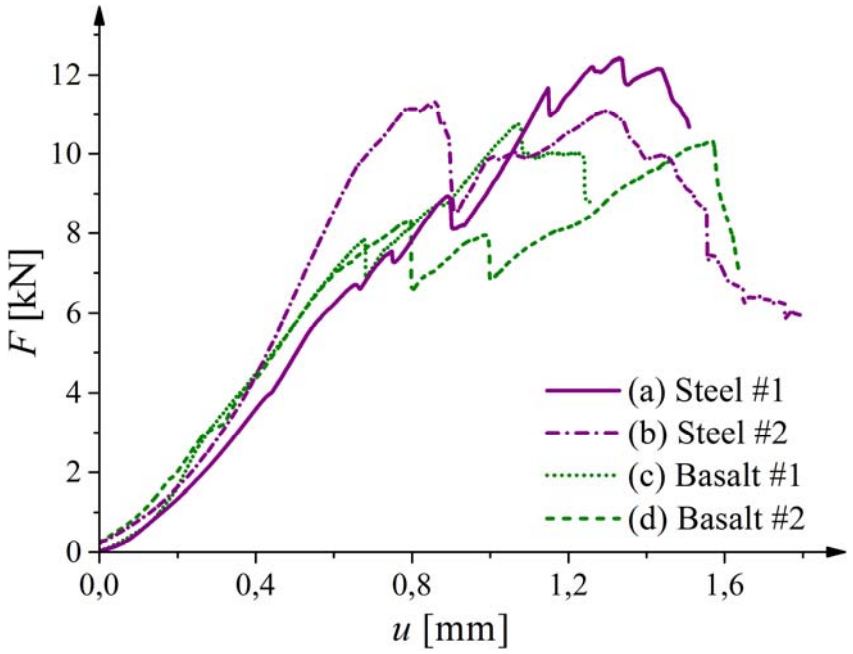

Figure 9: Experimental vertical force – deflection diagrams for concrete beams reinforced with (a), (b) steel and (c), (d) basalt reinforcement

The pattern of cracks on the back surface (not sprayed and photographed during DIC investigations) of the beams, observed before micro-CT scanning, are presented in Figures 10 and 11. Failure crack was strongly non-symmetric on both sides of beams in terms of the distance from the support and inclination to the horizontal line. The details of experimental results are presented in Table 5.

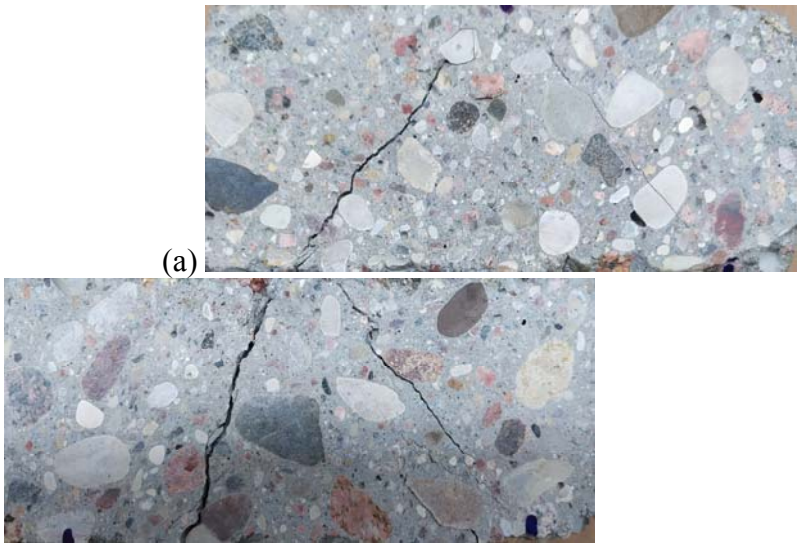

Figure 10: Crack patterns on the surface of concrete beams reinforced with steel bars: (a) Steel #1 and (b) Steel #2

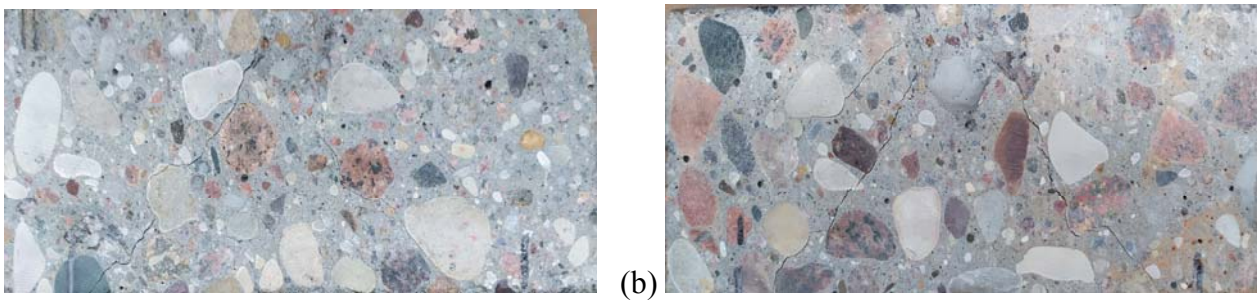

Figure 14: Crack patterns on the surface of concrete beams reinforced with basalt bars: (a) Basalt #1 and (b) Basalt #2

Table 5: Location and inclination of the failure crack in tested beams

Specimen number	Distance of failure crack from the support (front, sprayed side)	Inclination of failure crack (front, sprayed side)	Distance of failure crack from the support (back, not sprayed side)	Inclination of failure crack (back, not sprayed side)
Steel #1	0 mm	32^0	5 mm	45^0
Steel #2	5 mm	$28^0 – 90^0$	30 mm	72^0
Basalt #1	25 mm	56^0	10 mm	48^0
Basalt #2	3 mm	33^0	15 mm	56^0

The shear strength of the RC beams with a rectangular cross-section without shear reinforcement can be analytically calculated according to EC 1992-1-1:2004 [20], ACI 318 or alternative ACI method [21]. According to EC 1992-1-1:2004 [20], in case of elements without shear reinforcement, a following empirical formulae is proposed:

$$\tau_c^{EC} = \left[C_{Rd,c} k \left(100 \rho_1 f_c\right)^{1/3} \right] \qquad \text{where} \qquad k = 1 + \sqrt{\frac{200}{d}} \le 2 \tag{10}$$

wherein f_c – compressive strength of concrete, ρ_1 – reinforcement ratio (not greater than 0.02), d – effective height, a – distance of force from the support and b – beam width and k – size effect factor and $C_{R,dc}$=0,18. According to ACI 318 [21] shear strength can be calculated as follows:

$$\tau_c^{ACI} = 0.29\sqrt{f_c} \tag{11}$$

According to alternative ACI method [21] shear strength may be determined using following expression:

$$\tau_c^{ACI\,(alternative)} = 1.02 f_c \eta_c (1 - \eta_c) \frac{1}{\eta_a} \tag{12}$$

where $\eta_c = c/d$= 0.333 (for c=15 mm – distance from beam bottom to the center of reinforcement) and $\eta_a = a/d$=1.33. In the theoretical calculations, the following values were assumed: f_c=47.60 MPa, ρ_1=0.02 and d=0.045 m. The theoretical shear strength varied from 1.67 kN [20] to 8.29 kN [21] whereas the experimental ones varied from 2.86 kN to 3.45 kN. Calculations of shear strength following EC [20] and ACI [21] formulas underestimated whereas alternative ACI formulae [21] overestimated the experimental shear strength. Nevertheless, experimental results are within the range set by the standard formulas and observed discrepancies may be caused by a rather small geometry of the beams. The experimental and theoretical results were compared in Table 6.

Table 6: Shear strength $\tau_c = V_{max}/(bd)$ ($V_{max} = 0.5 P_{max}$) for RC beams according to EC2 (Eq. 10), ACI 318 (Eq. 11) and alternative ACI (Eq. 12)

Specimen number	**Shear strength from experiments τ_c^{exp} [MPa]**	**Shear strength by Eq. 10 [20] τ_c^{EC} [MPa]**	**Shear strength by Eq. 11 [21] τ_c^{ACI} [MPa]**	**Shear strength by Eq. 12 [21] $\tau_c^{ACI\ alternative}$ [MPa]**
Steel #1	3.45	1.67	2.00	8.29
Steel #2	3.15			
Basalt #1	2.99			
Basalt #2	2.86			

4.3. Fracture evolution by DIC

The displacement and strain changes on the beam surface were measured using the square inspection window with the dimension of 120 pixels and step between centers of the inspection windows equal 5 pixels. Figure 12 presents a vertical force F versus deflection u with marked points indicating image shot whereas Figure 13 shows main strain intensity on the surface of concrete beam reinforced with steel bar. Based on the analyses of strain distribution, a similar mechanism for all tested beams was observed. At first, close to the 50% of the maximum vertical force, bending crack appeared (Figure 13a). Appearance of bending crack resulted in a jump visible on the force-deflection curve (Figure 12). After that force began to increase once again until the inclined crack formed (Figures 13b and 13c). Afterwards, additional inclined cracks appeared (Figures 13d and 13e) and evolved in width and length up to the failure (Figure 13f). Figure 14 depicts comparison between micro-CT and

DIC experimental results on the surface of tested beams. Both methods revealed a very good similarity. Observed fracture zones appeared as vertical and inclined ones that were strongly curved due to presence of aggregate particles.

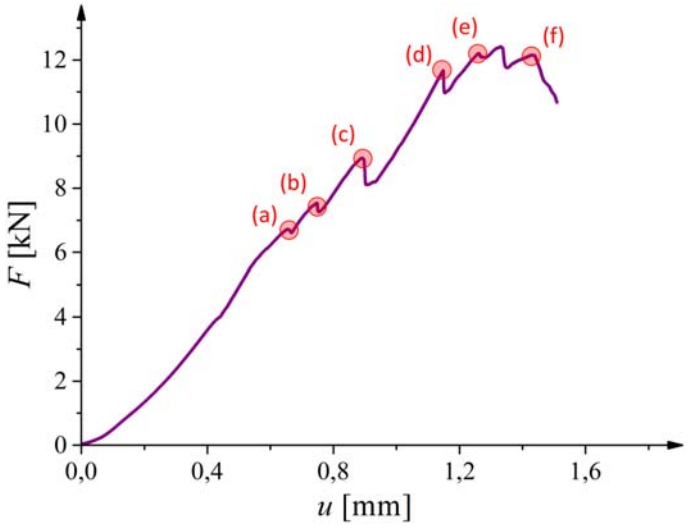

Figure 12: Experimental vertical force – deflection diagram for steel bar reinforced concrete beam with marked points indicating image shot

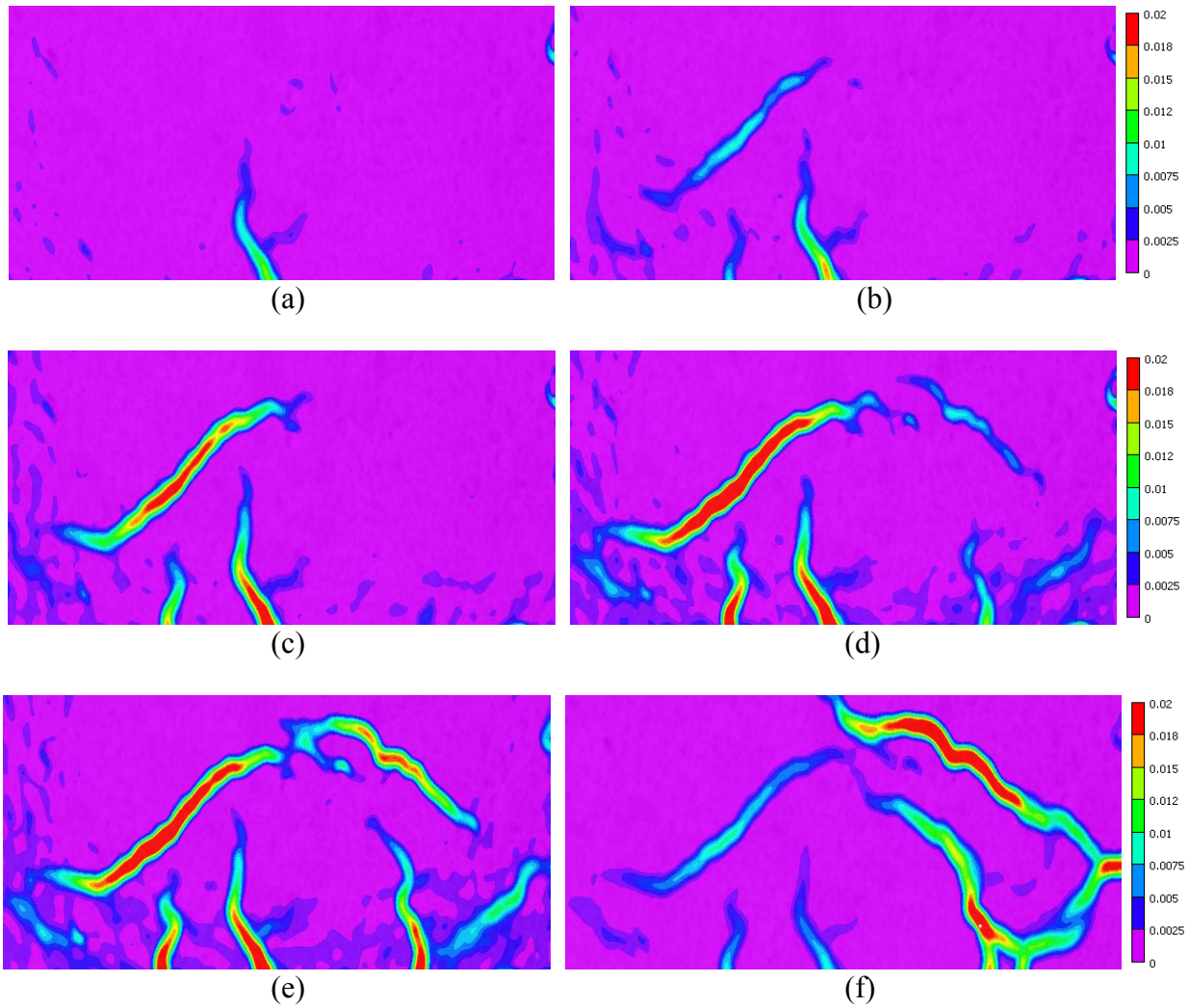

Figure 13:Evolution of fracture process on the surface concrete beam reinforced with steel bar (Steel #1) based on the main strain intensity map

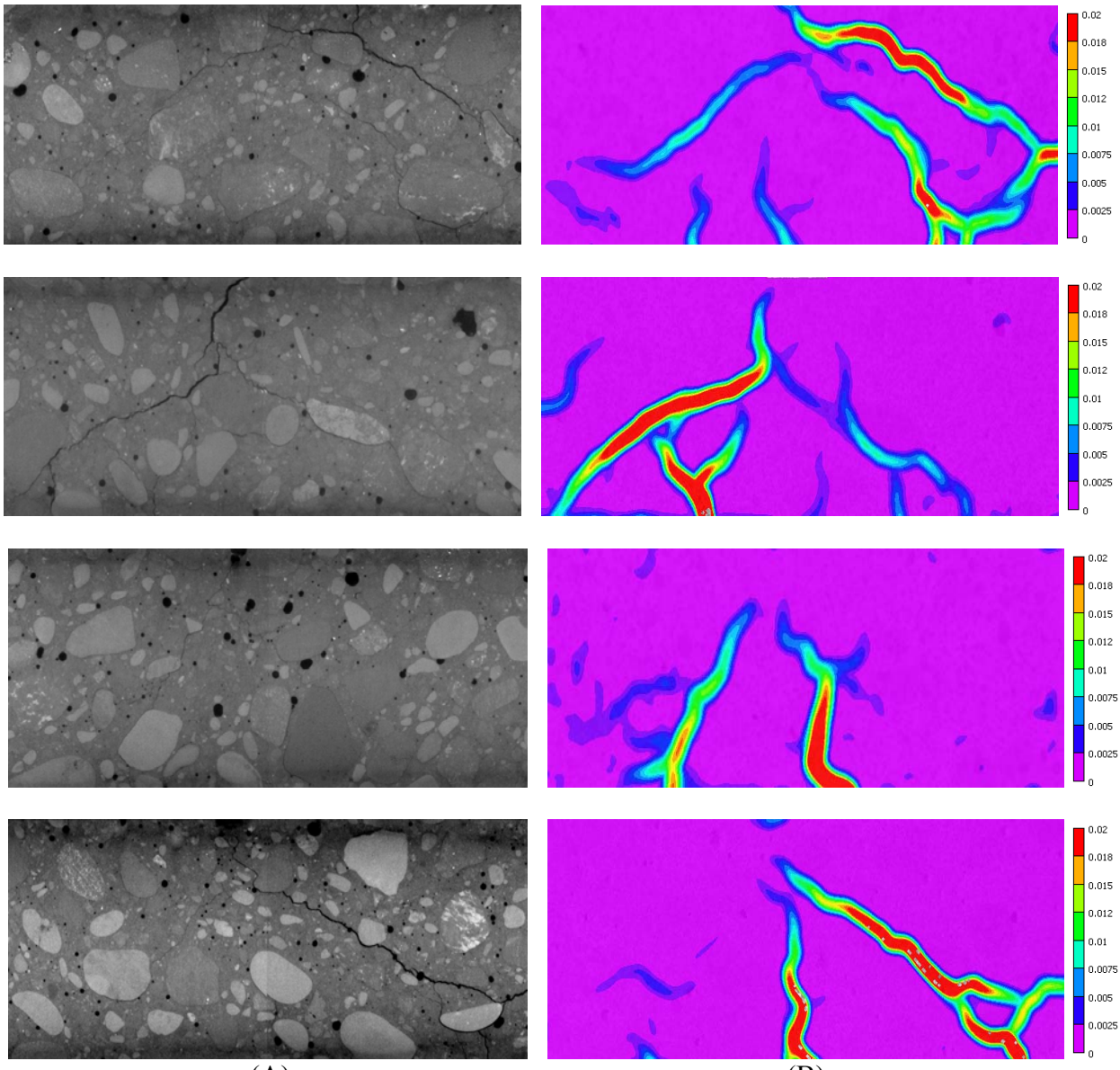

Figure 14: Comparison of: (A) micro-CT and (B) DIC technique results for concrete beams reinforced with (a), (b) steel bar (Steel #1 and #2) and (c), (d) basalt bar (Basalt #1 and #2)

4.4. Fracture phenomenon by micro-CT

Mechanism of failure during loading process was similar for concrete reinforced with steel and basalt bars. Cracks had a non-uniform width and were strongly curved along sample depth, width and height (Figures 15 and 16). Since the basalt bars have approximately the same density as cement matrix it was technically not possible to distinguish them from concrete and visualise in green like steel bars. The volume of cracks in concrete beams reinforced with steel bars was in the range from 7783.85 mm^3 to 11748.74 mm^3 that corresponds to 3.20% and 4.83% of the entire sample volume, whereas the volume of cracks in concrete beams reinforced with basalt bars was in the range from 11700.10 mm^3 to 14327.15 mm^3 that corresponds to 4.81% and 5.89% of the entire sample volume. It means that average volume of cracks in concrete beams reinforced with basalt bars equal 5.35% was by about 33% higher than the average volume of cracks in concrete beams reinforced with steel bars equal 4.01%. Maximum crack width in concrete beams reinforced with steel bars was equal

0.85 mm and 1.73 mm whereas in concrete beams reinforced with basalt bars was equal 1.24 mm and 1.46 mm, respectively. Average crack width in concrete beams reinforced with basalt bars equals 1.35 mm was by about 5% higher than the average crack width in concrete beams reinforced with steel bars equal 1.29 mm. Slightly higher value of average maximum crack width and visibly greater average volume of cracks in concrete beams reinforced with basalt bars might be caused by the larger average deflection observed in experiments. All experimental results concerning air pores volume, crack width and volume of cracks are presented in Table 7.

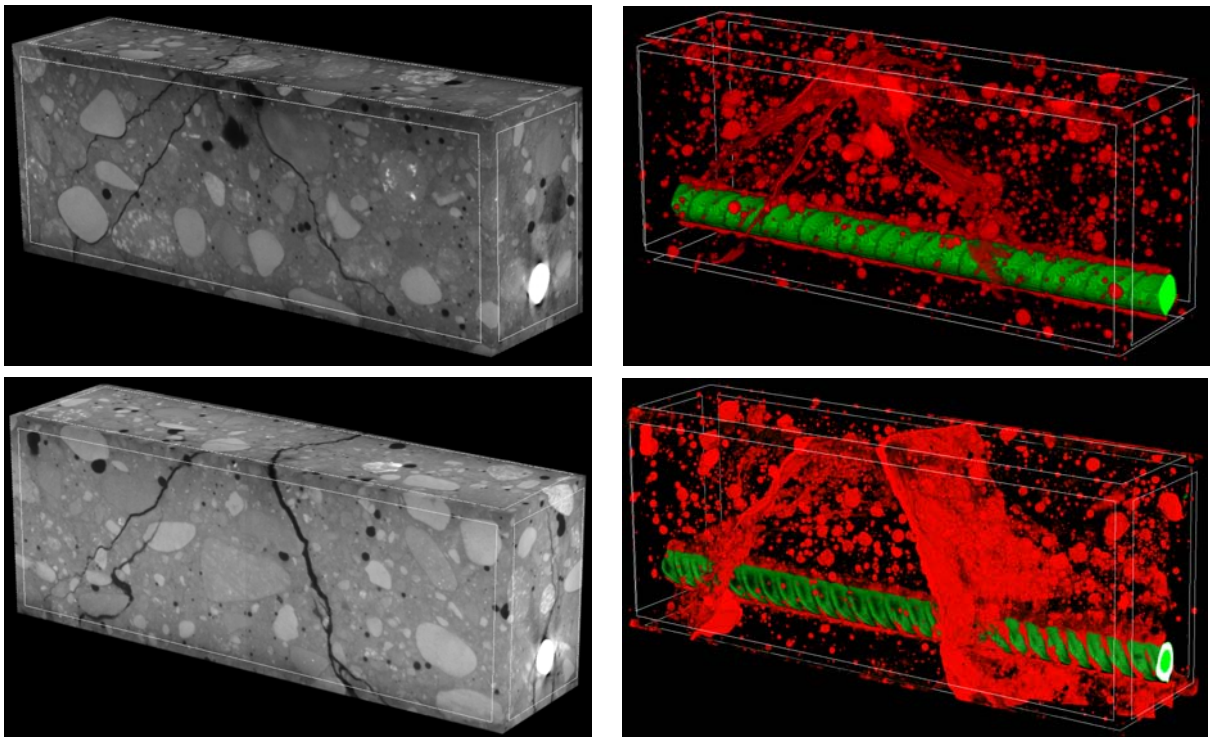

(a)

(b)

Figure 15: 3D micro-CT images of cracked concrete beams reinforced with steel bar: (a) Steel #1 and (b) Steel #2 (air pores and cracks in red, steel bar in green)

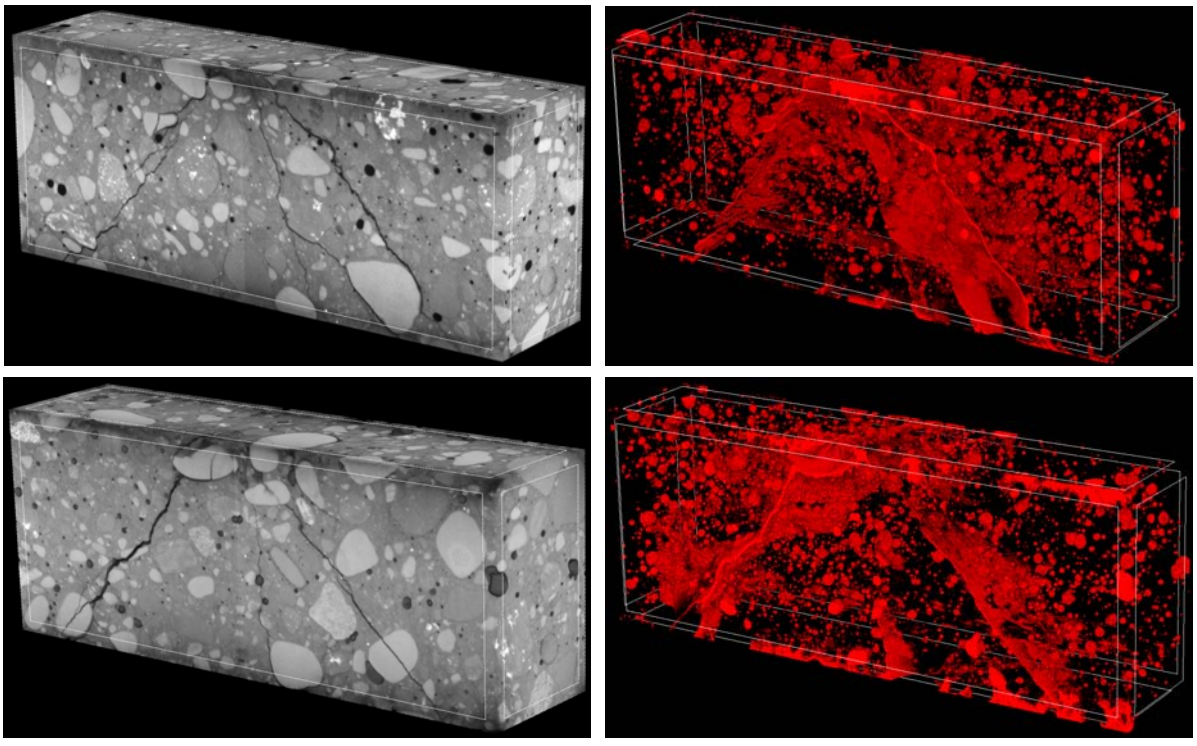

(a)

(b)

Figure 16: 3D micro-CT images of cracked concrete beams reinforced with basalt bar: (a) Basalt #1 and (b) Basalt #2 (air pores and cracks marked in red)

Table 7: Volume of pores, cracks and maximum crack width in reinforced concrete beams measured by micro-computed tomography

Specimen number	Volume of pores and cracks [mm^3]	Volume of pores and cracks [%]	Volume of cracks [mm^3]	Volume of cracks [%]	Maximum crack width [mm]
Steel #1	15202.83	6.25	7783.85	3.20	0.85
Steel #2	19313.67	7.94	11748.74	4.83	1.73
Basalt #1	20092.06	8.26	11700.10	4.81	1.24
Basalt #2	23132.63	9.51	14327.15	5.89	1.46

5. Numerical results and discussion

5.1. Macro-scale model

The FE results within macro-scale model are presented in Figures 17 and 18. Figure 17 shows numerically calculated force-displacement curves in comparison with experimental ones. The ultimate vertical forces are quite good reproduced in FE analyses using macro-scale approach. The maximum difference was 9.3% and 12.2% for beam with basalt and steel reinforcement, respectively. The numerically calculated values were higher than experimental ones and both FE curves were more stiff in comparison to curves from experiments. The contours of non-local equivalent strain measure are presented in Figure 18. In numerical calculations the critical diagonal shear localization zones were obtained for both beams, which is, in general, consistent with experimental crack pattern. The inclination of diagonal shear zone was 47° for basalt reinforcement and 42° for steel. Similar observation may be seen from experiments, i.e. critical cracks for beams with basalt reinforcement were steeper in comparison with cracks in beams with steel reinforcement. The average inclination (average value for front and back side for two specimens – Table 5) of failure cracks in experiments was 48° and 44° for beams with basalt and steel bars, respectively. The overall calculated number of localized zones was smaller in comparison with real i.e. experimental number of cracks. Moreover, in numerical calculations, in contrast with experiments, for both types of reinforcement the pronounce bending localized zone was observed in the central part of the beam.

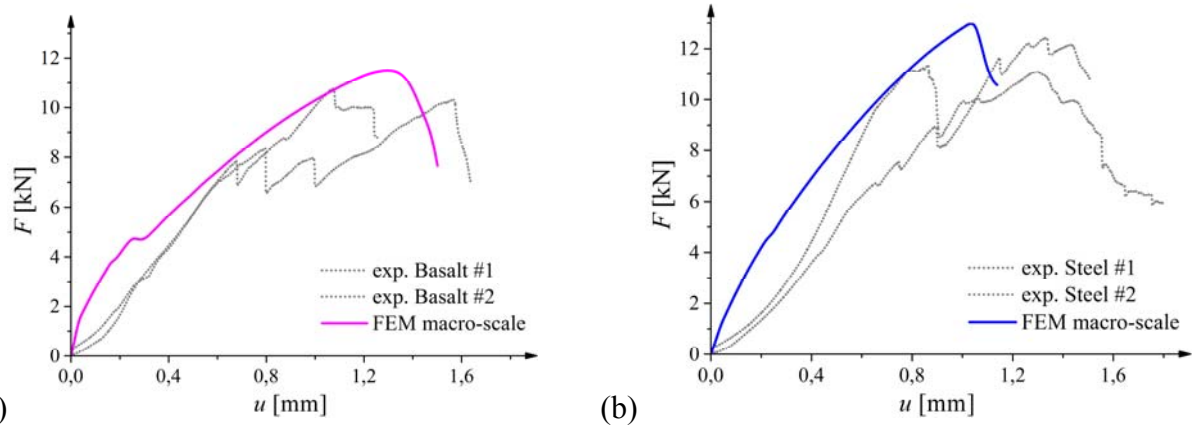

(a) (b)

Figure 17: Force – deflection curves for macro-scale model in comparison with experimental outcomes for beams with: (a) basalt and (b) steel reinforcement.

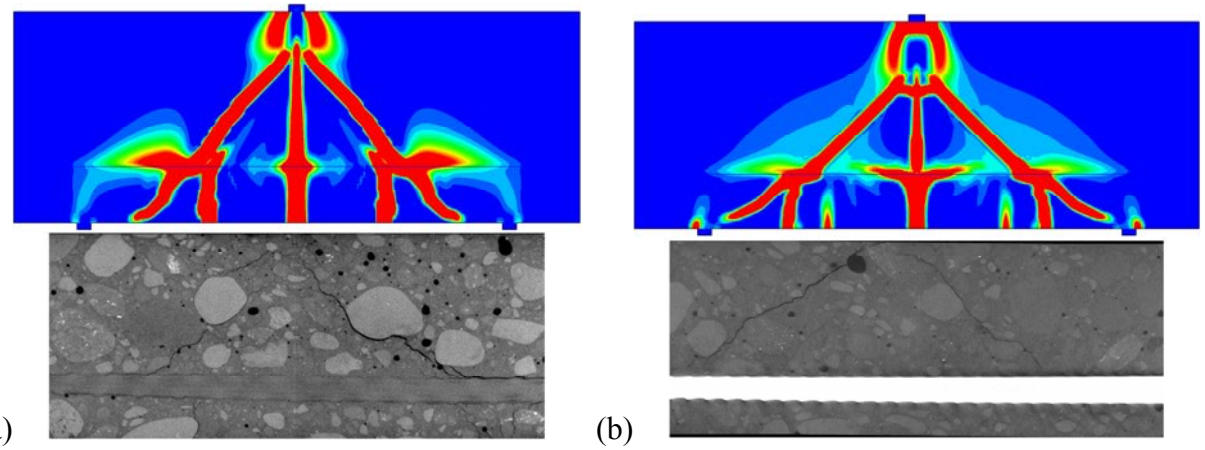

(a) (b)

Figure 18: Contours of non-local equivalent strain measure $\bar{\varepsilon}$ from macro-sale FE analyses compared with experimental cracks pattern at failure for beams with: (a) basalt and (b) steel reinforcement.

5.2. Meso-scale model

The FE results within meso-scale model are shown in Figures 19-21. Figure 19 shows comparison between numerically calculated force-displacement curves for all specimens and experimental curves. The ultimate vertical forces are better reflected using FE analyses with meso-scale approach than as it was obtained within macro-scale computations. The maximum difference was negligible since it were equal 5% and 5.2% for beam with basalt and steel reinforcement, respectively. The calculated curves are also less steep, thus the stiffness of overall response is better reproduced. Due to the representation of different meso-scale components in the FE analysis, the contours of strain localization (Figures 20-21) were different in comparison to macro-scale model (Figure 18). The larger number of localized zones was observed for all beams and the overall characteristic of crack pattern was better reflected. The shear zones propagated through the weakest components (mainly through ITZ zones that were the weakest parts of material) between aggregate grains that resulted in a curvature of cracks. In addition, a number of accompanying minor zones was observed which was consistent with experiments. The mechanism of cracking was satisfactorily reflected thus, similarly as in experiments, firstly a bending localised zones in the bottom central part of beams were observed and next, with increasing force, inclined zones started to form. Finally, further growth of inclined shear localised zones led to the failure. In contrast to macro-scale model, the bending zones were less developed. The calculated inclination of diagonal shear zone for basalt reinforced beams was 54° (Basalt #1) and 42° (Basalt #2) and it was with good agreement with experimental values (calculated as an average value for front and back side) equal 52° and 44°, respectively. In turn, for beams with steel reinforcement calculated inclination varied between 41° (Steel #1) and 49° (Steel #2) whereas average measured values were 38.5° (Steel #1) and 50° - 65.5° (Steel #2), respectively. Thus, the discrepancies concern mainly the beam Steel #2 where strongly curved shear zone was observed in experiment. Moreover, the shape of failure crack for Steel #2 was strongly non-uniform along beam's depth but in simulation only one cross section was analysed for this beam.

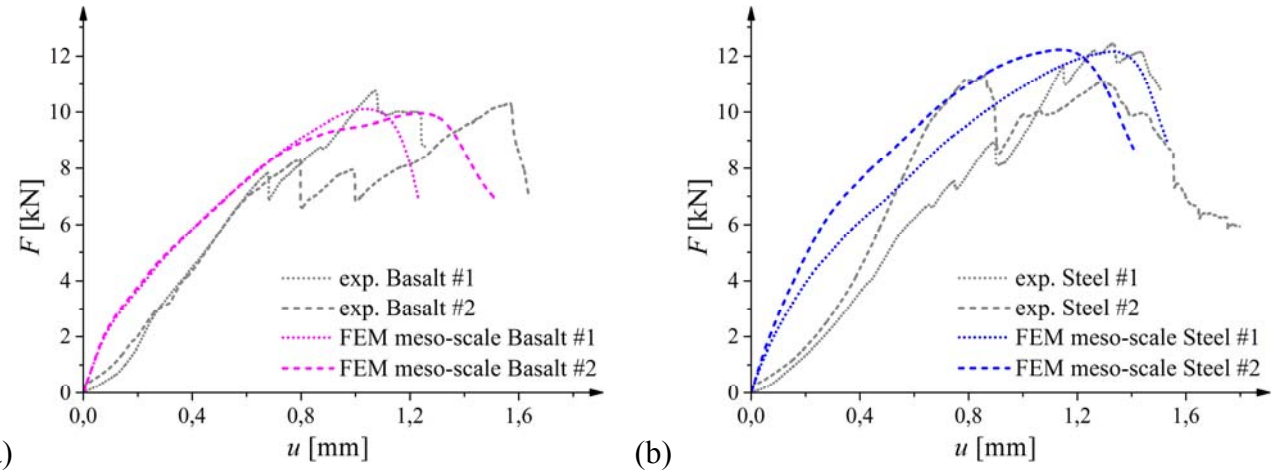

Figure 19: Force – deflection curves for meso-scale model in comparison with experimental outcomes for beams with: (a) basalt and (b) steel reinforcement.

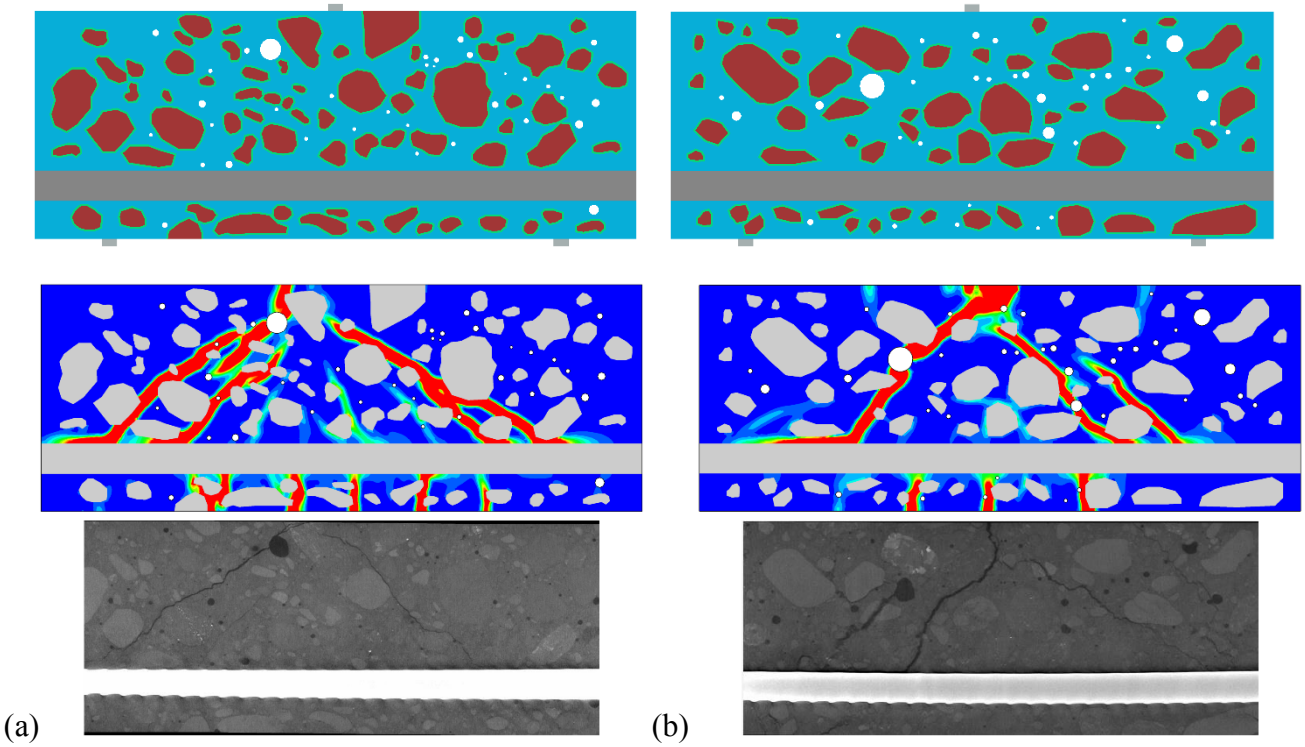

Figure 20: Numerical representation of meso-structure and contours of non-local equivalent strain measure $\bar{\varepsilon}$ from meso-scale FE analyses compared with experimental crack pattern at failure for beams with steel reinforcement: (a) Steel #1 and (b) Steel #2

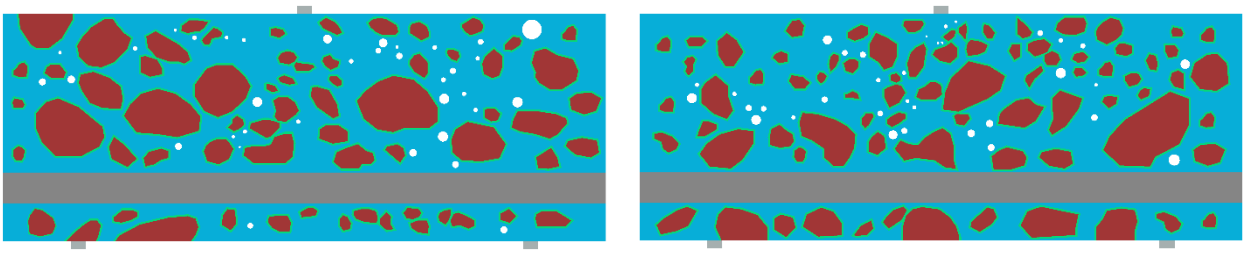

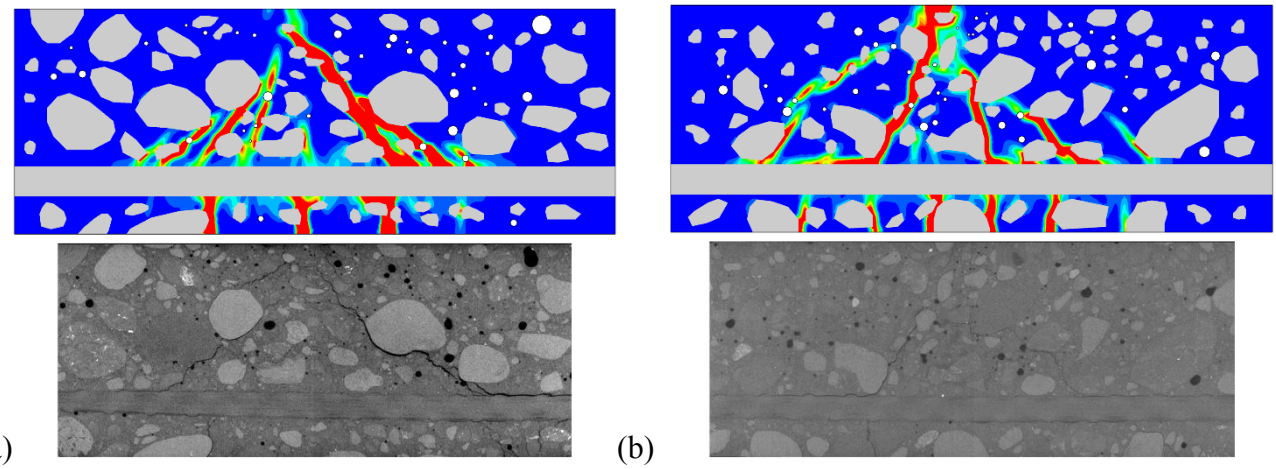

(a) (b)

Figure 21: Numerical representation of meso-structure and contours of non-local equivalent strain measure $\bar{\varepsilon}$ from meso-scale FE analyses compared with experimental cracks pattern at failure for beams with basalt reinforcement: (a) Basalt #1 and (b) Basalt #2

6. Conclusions

Numerical FE investigations of concrete reinforced with steel or basalt bars combined with the quantitative description of fracture phenomenon using Digital Image Correlation (DIC) and X-ray micro computed tomography (micro-CT) allow to draw the following conclusions:

(1) Average total porosity, measured by 3D micro-CT, of non-cracked concrete beams reinforced with steel bars (3.08%) was smaller by about 15% than porosity of non-cracked concrete beams reinforced with basalt bars (3.53%). Nevertheless, both values show a satisfactory agreement with air content of fresh concrete measured by means of the air pressure test (3.24%) that confirms reliability of that method.

(2) Micro-CT investigations revealed that, in spite of careful concreting and compacting of fresh mix, some free air along the steel bar ribs can be noticed. Presence of air along the steel bar ribs can lead to the deterioration of contact between concrete and reinforcement. This phenomenon was not observed in terms of basalt bar.

(3) During mechanical experiments, initially one or two bending cracks appeared close to the mid-span of tested beams and then inclined shear cracks occurred that continuously evolved in length and width along with the deformation process. Finally, failure took place in a rapid brittle way due to a diagonal shear crack moving through the beam compressive zone towards the loading point. Failure crack was strongly non-symmetric on both sides of beams in terms of the distance from the support and inclination to the horizontal line. Formation and evolution of cracks on the beams' surface was successfully observed using non-invasive Digital Image Correlation.

(4) The average experimental inclination of failure crack was approximately 48° and 44° whereas the average distance of failure crack from the support was approximately 13 mm and 10 mm for concrete beams reinforced with basalt and steel bars, respectively. That means that failure cracks in beams reinforced with basalt bars were steeper and placed farther from the support in comparison to beams reinforce with steel bars.

(5) Calculations of shear strength following EC (1.67 MPa) and ACI (2.00 MPa) formulas underestimated whereas alternative ACI formulae (8.29 MPa) overestimated the experimental

average shear strength (3.11 MPa) that was, in fact, similar for concrete beams reinforced with basalt and steel bars. Nevertheless, experimental results are within the range set by the standard formulas and observed discrepancies may be caused by a rather small geometry of tested beams.

(6) On the basis of 3D micro-CT measurements, the average volume of cracks in beams reinforced with basalt bars (5.35%) was by about 33% higher than in concrete beams reinforced with steel bars (4.01%). At the same time, the average crack width in concrete beams reinforced with basalt bars (1.35 mm) was by about 5% higher than in concrete beams reinforced with steel bars (1.29 mm). Slightly higher value of average maximum crack width and visibly greater average volume of cracks in concrete beams reinforced with basalt bars might be caused by the larger average deflection observed in experiments.

(7) The FE macro-scale modelling using non-local coupled isotropic elasto-plastic-damage model for concrete ensures the acceptable compliance with experimental outcomes. This approach provides proper estimation regarding to calculated load-bearing capacity and overall characteristic of failure mechanism in reinforced concrete beams with relatively little time expenditure for numerical calculations.

(8) The FE meso-scale model allows to go into details of the curvature and heterogeneity of critical shear zones with taking into account the real material meso-structure. As a consequence, the improvement in calculated ultimate vertical forces and overall stiffness of beams response was achieved. Moreover, representation of different meso-scale components in FE calculations leads to obtain more realistic shape of calculated crack patterns.

(9) The advantage of advanced coupled elasto-plastic-damage meso-scale modelling to comprehensively study the mechanism of the initiation, growth and formation of localized zones and cracks was confirmed.

7. Future perspectives

This paper presents preliminary numerical 2D simulations of reinforced concrete beam subjected to 3-point bending where only aggregate grains of diameter $\geq$ 2 mm were modelled and satisfactory agreement with experimental investigations has been achieved. In order to make further improvements, 2D and 3D investigations with aggregate diameters $\geq$ 0.5 mm will be carried out.

References

[1] Morrow I., Viest I. (1956) Shear strength of reinforced concrete frame members without web reinforcement. *Journal of the ACI*, **53 (9)**, pp. 833-870.

[2] Mathey R. G., Watstein D. (1963) Shear strength of beams without web reinforcement containing deformed bars of different yield strengths. *Journal of the ACI,* pp. 183-207.

[3] Kani G. N. J. (1964) The riddle of shear failure and its solution. *Journal of the ACI*, **61 (4)**, pp. 441-467.

[4] Kani G. N. J. (1966) Basic facts concerning shear failure. *Journal of the ACI*, **63 (6)**, pp. 675-692.

[5] Krefeld W. J., Thurston C. (1966) Contribution of longitudinal steel to shear resistance of reinforced concrete beams. *Journal of the ACI*, **63 (3)**, pp. 325-344.

[6] Krefeld W. J., Thurston C. (1966) Studies of shear and diagonal tension strength of simply supported reinforced concrete beams. *Journal of the ACI*, **63 (4)**, pp. 451-476.

[7] Leonhardt F., Walther R. (1966) Contribution of longitudinal steel to shear resistance of reinforced concrete beams. *Deutscher Ausschuß für Stahlbeton,* **151**.
[8] Kani G. N. J. (1967) How safe are our large reinforced concrete beams. *ACI Journal*, **64 (3)**, pp. 128-141.
[9] Rajagopolan K. S., Ferguson P. M. (1968) Exploratory shear tests emphasizing percentage of longitudinal steel. *ACI Journal*, **65 (8)**, pp. 634-638.
[10] Zsutty T. (1971) Shear strength prediction for separate categories of simple beam tests. *ACI Journal,* **68 (2)**, pp. 138-143.
[11] Bažant Z., Kazemi M. T. (1991) Size effect on diagonal shear failure of beams without stirrups. *ACI Structural Journal*, **88 (3)**, pp. 268-276.
[12] Walraven J., Lehwalter N. (1994) Size effects in short beams loaded in shear. *ACI Structural Journal*, **91 (5)**, pp. 268-276.
[13] Hamrat H., Boulekbache B., Chemoruk M., Amziane S. (2010) Shear behaviour of RC beams without strirrups made of normal strength and high strength concretes. *Advances in Structural Engineering*, **13 (1)**, pp. 29-41.
[14] Słowik M. (2010) Analysis of shear failure in reinforced concrete beams without stirrups. *Journal of Civil Engineering and Architecture*, **4/8**, pp. 59-64.
[15] Słowik M., Smarzewski P. (2012) Study on the scale effect on diagonal crack propagation in concrete beams. *Computational Materials Science*, **64**, pp. 216-220.
[16] Caldentey A. P., Padilla P., Muttoni A., Ruiz M. F. (2012) Effect of load distribution and variable depth on shear resistance of slender beams without stirrups. *ACI Structural Journal*, **109 (5)**, pp. 595-603.
[17] Jaeger T. (2013) Extended sandwich model for reinforced concrete slabs: Shear strength without transverse reinforcement. *Engineering Structures*, **55**, pp. 1142-1153.
[18] Perera S. V. T., Mutsuyoshi H. (2013) Shear behaviour of reinforced high-strength concrete beams. *ACI Structural Journal*, **110 (1)**, pp. 43-52.
[19] Suchorzewski J., Korol E., Tejchman J., Mróz Z. (2018) Experimental study on shear strength and failure mechanisms in RC beams scaled along height or length. *Construction and Building Materials,* **157**, pp. 203-223.
[20] EN 1992-1-1:2004 Design of concrete structures. Part 1: General rules and rules for buildings.
[21] ACI Committee 318 (2002) Building Code Requirements for Structural Concrete (ACI 318-02) and Commentary (ACI 318R-02).
[22] ACI Committee 224R-01 (2001) Control of Cracking in Concrete Structures.
[23] ACI Committee 435R-01 (2000) Control of Deflection in Concrete Structures.
[24] Skarżyński Ł. and Tejchman J. (2013) Experimental investigations of fracture process using DIC in plain and reinforced concrete beams under bending. *Strain*, **49 (6)**, pp. 521-543.
[25] Suchorzewski, J., Tejchman, J., Nitka, M. (2018) Experimental and numerical investigations of concrete behaviour at meso-level during quasi-static splitting tension. *Theoretical and Applied Fracture Mechanics*, **96**, pp. 720-739.
[26] Skarżyński, Ł., Suchorzewski, J. (2018) Mechanical and fracture properties of concrete reinforced with recycled and industrial steel fibers using Digital Image Correlation technique and X-ray micro computed tomography. *Construction and Building Materials*, **183**, pp. 283-299.
[27] Skarżyński Ł. (2020) Mechanical and radiation shielding properties of concrete reinforced with boron-basalt fibers using Digital Image Correlation and X-ray micro-computed tomography, Construction and Building Materials, **255**, https://doi.org/10.1016/j.conbuildmat.2020.119252.
[28] Suchorzewski, J., Tejchman, J., Nitka, M. (2018) DEM simulations of fracture in concrete under uniaxial compression based on its real internal structure. *International Journal Damage Mechanics*, **27 (4)**, pp. 578-607.
[29] Skarżynski Ł., Marzec I. and Tejchman J. (2018) Crack evolution in concrete compressive fatigue experiments based on X-ray micro-CT images. *International Journal of Fatigue,* **122**, pp. 256-272.

[30] Skarżyński Ł., Tejchman J. (2016) Experimental investigations of fracture process in concrete by means of X-ray micro-computed tomography. *Strain*, **52 (1)**, pp. 26-45.
[31] Ponikiewski, T., Katzer, J., Bugdol, M. and Rudzki, M. (2015) X-ray computed tomography harnessed to determine 3D spacing of steel fibers in self compacting (SCC) slabs. *Construction and Building Materials*, **74**, pp. 102-208.
[32] Balázs, G. L., Czobly, O., Lublóy, E., Kaplitány, K. and Barsi, A. (2017) Observation of steel fibers in concrete with Computed Tomography. *Construction and Building Materials,* **140**, pp. 534-541.
[33] Yua Q., Liub H., Yanga, T. and Liua, H. (2018) 3D numerical study on fracture process of concrete with different ITZ properties using X-ray computerized tomography. *International Journal of Solids and Structures,* **147**, pp. 204-222.
[34] Loeffler, C. M., Qiua Y., Martin B., Heard W., Williams B., Niea X. (2018) Detection and segmentation of mechanical damage in concrete with X-ray microtomography. *Materials Characterization,* **142**, pp. 515-522.
[35] Vicente, M. A., Ruiz, G., Gonzalez, D. C., Mínguez, J., Tarifa, M. and Zhang, X. X. (2018) CT-Scan study of crack patterns of fiber-reinforced concrete loaded monotonically and under low-cycle fatigue, *International Journal of Fatigue,* **114**, pp. 138-147.
[36] Vicente M.A., Mínguez J., and Gonzalez D.C. (2019) Computed tomography scanning of the internal microstructure, crack mechanisms and structural behaviour of fiber-reinforced concrete under static and cyclic bending tests, *International Journal of Fatigue,* **121**, pp. 1-19.
[37] Ríos, J. D., Leive, C., Ariza, M. P., Seitl, S. and Cifuentes, H. (2019) Analysis of the tensile fracture properties of ultra-heigh-strength fiber-reinforced concrete with different types of steel fibers by X-ray tomography. Materials and Design, **165**, pp. 1-14.
[38] Skarżyński Ł. and Tejchman J. (2019) Experimental investigations of damage evolution in concrete during bending by continuous micro-CT scanning. *Materials Characterization,* **154**, pp. 40-52.
[39] Menétrey P., Willam K.J. (1995) Triaxial failure criterion for concrete and its generalization. *ACI Structural Journal*, **92 (3)**, pp. 311-318.
[40] Feenstra P.H., de Borst R. (1996) A composite plasticity model for concrete. *International Journal of Solids and Structures*, **33 (5)**, pp. 707-730.
[41] Meschke G., Lackner R., Mang H.A. (1998) An anisotropic elastoplastic-damage model for plain concrete. *International Journal for Numerical Methods in Engineering*, **42 (4)**, pp. 702-727.
[42] Pivonka P., Ožbolt J., Lackner R., Mang H. (2004) Comparative studies of 3D-constitutive models for concrete: application to mixed-mode fracture. *International Journal for Numerical Methods in Engineering*, **60 (2)**, pp. 549–570.
[43] Desmorat R., Gatuingt F., Ragueneau F. (2007) Nonlocal anisotropic damage model and related computational aspects for quasi-brittle materials. *Engineering Fracture Mechanics*, **74 (10)**, pp.1539-1560.
[44] Grassl P., Xenos D., Nystrom U., Rempling R., Gylltoft K. (2013) CDPM2: a damage-plasticity approach to modelling the failure of concrete. *International Journal of Solids and Structures*, **50**, pp. 3805-3816.
[45] Ortiz M., Pandolfi A. (1999) Finite-deformation irreversible cohesive elements for three-dimensional crack propagation analysis. *International Journal for Numerical Methods in Engineering*, **44(9)**, pp. 1267-1282.
[46] Zhou F., Molinari J.F. (2004) Dynamic crack propagation with cohesive elements: a methodology to address mesh dependency. *International Journal for Numerical Methods in Engineering*, **59(1)**, pp. 1-24.
[47] Xue, C, Li, W., Li, J. and Wang, K. (2019) Numerical investigation on interface crack initiation and propagation behaviour of self-healing cementitious materials. *Cement and Concrete Research*, **122**, pp. 1-16

[48] Welss G.N., Sluys L.J. (2001) A new method for modelling cohesive cracks using finite elements. *International Journal for Numerical Methods in Engineering*, **50(12)**, 2667-2682.
[49] Moes N., Belytschko T. (2002) Extended finite element method for cohesive crack growth. *Engineering Fracture Mechanics*, **69(7)**, 813-833.
[50] Nguyen T. T., Yvonnet J., Bornert M. and Chateau C. (2016) Initiation and propagation of complex 3D networks of cracks in heterogeneous quasi-brittle materials: Direct comparison between in situ testing-microCT experiments and phase field simulations. *Journal of the Mechanics and Physics of Solids*, **95**, pp. 320-350
[51] Huang Y., Yan D., Yang Z. and Liu G. (2016) 2D and 3D homogenization and fracture analysis of concrete based on in-situ X-ray Computed Tomography images and Monte Carlo simulations. *Engineering Fracture Mechanics,* **163**, pp. 37-54.
[50] Yang Z., Ren W., Sharma R., McDonald S., Mostafavi M., Vertyagina Y., Marrow, T. J. (2017) In-situ X-ray computed tomography characterization of 3D fracture evolution and image-based numerical homogenization of concrete. *Cement and Concrete Composites*, **75**, pp. 74-83.
[53] Khormani M. Kalat Jaari V. R., Aghayan I., Ghaderi S. H. and Ahmadyfard A. (2020) Compressive strength determination of concrete specimens using X-ray computed tomography and finite element method. *Construction and Building Materials*, doi.org/10.1016/j.consbuildmat.2020.119427
[54] Skarżyński Ł., Nitka M., Tejchman J. (2015). Modelling of concrete fracture at aggregate level using FEM and DEM based on X-ray micro-CT images of internal structure. *Engineering Fracture Mechanics*, **147**, pp. 13-35
[55] Nitka M. and Tejchman J. (2018) A three-dimensional meso-scale approach to concrete fracture based on combined DEM with X-ray μCT images. *Cement and Concrete Research*, **107**, pp. 11-29.
[56] Suchorzewski J., Tejchman J. and Nitka M. Modelling of concrete behaviour in uniaxial compression and tension with DEM. *Granullar Matter*, **17 (1)**, pp. 45-64.
[57] Tan, X., Li, W. Zhao, M. and Tam, V. (2019) Numerical Discrete-Element Method Investigation on Failure Process of Recycled Aggregate Concrete. *Journal of Materials in Civil Engineering*, **31(1)**, 04018353.
[58] EN 12350-7:2009 Testing fresh concrete. Air content. Pressure methods.
[59] EN 12390-2:2009 Testing hardened concrete – Part 2: Making and curing specimens for strength tests.
[60] EN 12390-3:2009 Testing hardened concrete – Part 3: Compressive strength of test specimens.
[61] EN 12390-6:2011 Testing hardened concrete – Part 6: Tensile splitting strength of test specimens.
[62] EN 14651:2005+A1:2007 Test method for metallic fiber concrete. Measuring the flexural tensile strength (limit of proportionality (LOP), residual).
[63] Marzec, I., Tejchman, J., Mróz, Z. (2019) Numerical analysis of size effect in RC beams scaled along height or length using elasto-plastic-damage model enhanced by non-local softening. *Finite Elements in Analysis and Design*, **157**, pp. 1-20.
[64] Marzec, I., Skarżyński, Ł, Bobiński, J., Tejchman, J. (2013) Modelling reinforced concrete beams under mixed shear-tension failure with different continuous FE approaches. *Computers and Concrete*; **12 (5)**, pp. 585-612.
[65] Skarżyński, Ł., Marzec, I., Tejchman, J. (2017) Experiments and numerical analyses for composite RC-EPS slabs. *Computers and Concrete*, **20 (6)**, pp. 689-704.
[66] Skarżyński, Ł., Marzec, I., Drąg, K., Tejchman, J. (2018) Numerical analyses of novel prefabricated structural wall panels in residential buildings based on laboratory tests in scale 1:1. *European Journal of Environmental and Civil Engineering*, doi.org/10.1080/19648189.2018.1474382.
[67] Pamin, J., de Borst, R. (1999) Stiffness degradation in gradient-dependent coupled damage-plasticity. *Archives of Mechanics*, **51 (3-4)**, pp. 419–446.

[68] Mazars, J. (1986) A description of micro- and macroscale damage of concrete structures. *Engineering Fracture Mechanics*, **25 (5-6)**, pp. 729–737.
[69] Lee, J., Fenves, G. L. (1998) Plastic-damage model for cyclic loading of concrete structures. *Journal of Engineering Mechanics ASCE*, **124 (8)**, pp. 892–900.
[70] Pereira, L., Weerheijm, J., Sluys, L.A. (2017) A numerical study on crack branching in quasi-brittle materials with a new e□ective rate-dependent nonlocal damage model. *Engineering Fracture Mechanics*, **182**, pp. 689–707.
[71] Peerlings, R. H. J., de Borst, R., Brekelmans, W. A. M., Geers, M. G. D. (1998) Gradient enhanced damage modelling of concrete fracture, *Mechanics of Cohesive-Frictional Materials*, **3**, pp. 323-342.
[72] Geers, M.G.D. (1997) Experimental Analysis and Computational Modeling of Damage and Fracture, *PhD Thesis*, Eindhoven University of Technology.
[73] Xenos, D., Grégoire, D., Morel, S., Grassl, P. (2015) Calibration of nonlocal models for tensile fracture in quasi-brittle heterogeneous materials. *Journal of the Mechanics and Physics of Solids,* **82**, pp. 48–60.
[74] Grassl, P., Xenos, D., Jirásek, M., Horák, M. (2014) Evaluation of nonlocal approaches for modelling fracture near nonconvex boundaries. *International Journal of Solids and Structures*; **51**, pp. 3239-3251.
[75] CEB-FIP, CEB-FIP Model Code 1990, 1993.
[76] Abaqus Documentation (2016), Dassault Systemes.